Large-scale density functional theory simulations of defects and hydrogen incorporation in PuO_2

Nabeel Anwar,[1] Robert M. Harker,[2] Mark T. Storr,[2] Marco Molinari,[3] and Chris-Kriton Skylaris[1,*]

[1]*School of Chemistry, University of Southampton, Southampton SO17 1BJ, United Kingdom*

[2]*AWE, Aldermaston, Reading RG7 4PR, United Kingdom*

[3]*Department of Physical and Life Sciences, University of Huddersfield, Huddersfield HD1 3DH, United Kingdom*

(Received 17 January 2024; accepted 17 April 2024; published xxxxxxxxxx)

We have examined a range of point defects, Frenkel pairs, Schottky defects, and hydrogen-related defects in the PuO_2 system (supercells of 96 and 768 atoms) using the ONETEP linear-scaling density functional theory code. Vacancy point defects related to oxygen are found to be more stable than those related to plutonium. The oxygen in the octahedral interstitial is higher in the formation energy than the plutonium in the same octahedral site, although the difference is less than 1 eV. We were also able to identify a stable peroxide species (1.57–2.67 eV) with a O-O distance of 1.46 Å. Of the Frenkel defects we studied, we found that the oxygen is more stable than the plutonium, whereas the Schottky stability changes as a function of supercell size. Finally, we examined a number of likely hydrogen sites in the PuO_2 lattice: octahedral interstitial, oxygen edge, hydroxyl, oxygen vacancy, and plutonium vacancy. We report hydrogen which exists as a hydride at oxygen and plutonium vacancies to be relatively high in energy (2.69–3.81 and 13.71–15.54 eV, respectively). The hydrogen was found to exist as a radical at the octahedral interstitial site (2.43–3.38 eV) and which is somewhat higher formation energy than other studies find. We find that the hydrogen at the oxygen edge (as a H^+ cation) and at the oxygen cube corner (as a hydroxyl) are both lower in energy (1.14–1.40 and 1.17–1.56 eV, respectively) as opposed to hydrogen in the octahedral interstitial site but again higher than found by other studies. We discuss the data in the context of potential hydrogen transport pathways and how that might be modified by radiation damage.

DOI: 10.1103/PhysRevB.00.004100

I. INTRODUCTION

Plutonium is an important material on account of its ability to fission and generate power. Typically, plutonium is encountered as the stable plutonium dioxide (PuO_2) form, in civil nuclear fuels [1] on its own and within mixed oxides (MOX), and is generally also in the PuO_2 form for long-term storage [2]. In its metallic form, plutonium, due to its oxophilic nature, quickly develops an oxide film on the metal that slows further oxidation [3,4]. The oxide overlayer film acts as a barrier since reactive species, such as oxygen and hydrogen, are required to transport across the oxide barrier in order to react with the metal.

Plutonium is also radioactive with the majority of its isotopes and daughter products decaying through α radiolysis. Both the emitted α particles (helium nuclei of energy 4.8–5.5 MeV) and the recoil atoms (uranium from plutonium isotopes of energy 82–94 keV) create defect damage but over different length scales [5,6]. Considering the α-radiation damage in both bulk and in overlayers of PuO_2, the α particle has a range of approximately 10 μm losing energy by electronic stopping: defects produced are largely isolated Frenkel pairs with little annihilation or clustering of the defects [7]. Predictions suggest up to 66 cation [plutonium Frenkel (PuF)] and 140 anion [oxygen Frenkel (OF)] displacements due to an α particle ejected from ^{238}Pu [5]. The daughter recoil atom has less energy but loses it by nuclear stopping processes over a much shorter distance of 6–20 nm (less than 0.2% of the distance of the α particle) creating a far more concentrated defect volume [2]. Calculations suggest up to 140 cation and 1180 anion displacements from the recoil atom. The in-growth of radiation-induced defects, helium, and daughter products changes the material over time and with it the material physical and mechanical properties [7–9].

Molecules, radicals, and ions must traverse any oxide barrier to react with the underlying plutonium metal. Since the defect density in the oxide changes as a function of time, it then follows that the barrier properties of the oxide overlayer may be affected by the in-growth of defects. A particular example is that of the reaction of hydrogen with plutonium metal in storage environments [4,10–14]. This reaction is thought to be governed exclusively by the barrier diffusion process [15] in the earliest stages of the reaction, such as during the "induction phase" [16,17]. The reaction of hydrogen with plutonium can produce hazardous plutonium hydride [18–22]. Thus, understanding the relationship between PuO_2 defects and the transport of hydrogen through this oxide allows for a better prediction of how much plutonium hydride might be produced in storage.

Plutonium dioxide adopts the calcium fluoride (CaF_2) crystal structure, with the $Fm\bar{3}m$ space group [23]. In this structure, the oxygen anions are in a simple cubic packing within the unit cell which is bounded by plutonium cations at the cell corners and the face-centered positions. The plutonium cations make up the face-centered-cubic (fcc) arrangement and the oxygen anions are located at the tetrahedral interstices leaving the octahedral sites vacant. Each plutonium

*c.skylaris@soton.ac.uk

cation coordinates to eight oxygen anions whereas each oxygen anion coordinates to four plutonium cations. The oxide is an insulator with a band gap measured at 1.80 eV [24,25] and 2.80 eV [26] and a wealth of evidence confirming a diamagnetic (DM) ground state [27–31]. First-principle methods generally calculate a ferromagnetic (FM) or antiferromagnetic (AFM) ground state [32–38].

Computational studies of PuO_2 are challenging due to the highly correlated and localized nature of f electrons [39–42]. Standard density functional theory (DFT) [43,44] fails to produce the correct electronic structure, often underestimating the band gap of actinide oxide (AnO_2) materials, treating them as metallic instead of insulators [24,45]. The local-density approximation (LDA) and generalized gradient (GGA) approximation functionals alone do not capture the localization arising from the strong electron-electron interactions. Hybrid functionals more accurately describe the f states [45–48], however, these are computationally expensive. Alternatively, DFT+U is a more feasible method to account for the onsite Coulomb repulsion of the f electrons by adjusting the U parameter [49–51].

The unfavorable, cubic scaling of conventional DFT limits computational studies into PuO_2 properties [32,33,37,38,45,52–54] and defect formation [13,14,55–57] to small supercells. Smaller simulation cells suffer from stronger finite-size effects [58,59], such as increased strain around a defect site [60–62]. Finite-size effects are minimized with larger system sizes, using linear-scaling DFT methods which overcome the unfavorable scaling of conventional DFT with increasing system size. The crossover point, where linear-scaling DFT methods become more efficient than conventional DFT, typically lies on the order of hundreds of atoms [63]. ONETEP(order-N electronic total energy package) [64] uses a reformulation of DFT, based on the one-particle density matrix $\rho(\mathbf{r}, \mathbf{r}')$. The locality or nearsightedness of the density matrix exploited [65,66], by expanding the localized orbitals as nonorthogonal generalized Wannier functions (NGWFs) in the basis of periodic sinc (psinc) functions [67,68]. These NGWFs are self-consistently optimized during the energy minimization.

In this work, we investigate a range of intrinsic and extrinsic defects in bulk PuO_2. We expand the simulation cell up to 768 atoms to study point, Frenkel, and Schottky defects using ONETEP. By increasing the supercell size, we can isolate and dilute the concentration of point defects to minimize finite-size effects. We use the larger simulation cells to determine the energetic ordering of the Frenkel defects and Schottky defects. The incorporation of the hydrogen into bulk PuO_2 at the interstitial and substitutional positions within the material is also investigated. Hydrogen can exist as a cation (H^+), hydride (H^-), or a radical within solid materials, with limited reports on which species could be present in bulk PuO_2 [11–14,69]. Experimentally, it is currently undetermined as to which hydrogen species could be present in PuO_2.

II. METHODOLOGY

A. Computational details

Optimizations of stoichiometric and defective PuO_2 were performed using the ONETEP linear-scaling DFT package [64]. Calculations were performed using the Perdew-Burke-Ernzerhof (PBE) [70] generalized gradient approximation (GGA) exchange-correlation functional. The valence electrons for hydrogen ($1s^1$), oxygen ($2s^2 2p^4$), and plutonium ($6s^2 6p^6 7s^2 5f^6 6d^0$) were treated using a plane-wave basis set, with a kinetic energy cutoff of 900 eV, whereas the core electrons were frozen in the norm-conserving pseudopotential (NCP) on-the-fly generated (OTFG) using the CASTEP code [71]. Initially, the 2×2×2 supercell of the 12-atom unit cell containing 96 simulation cells was optimized using plane-wave DFT (CASTEP), with a 4×4×4 Monkhorst-Pack k-points mesh [72] to sample the Brillouin zone. The larger 4×4×4 supercells containing 768 atoms were generated from the optimized 2×2×2 supercell.

For all simulations, the system was considered as spin polarized, and spin-orbit coupling was not included to minimize computational cost. Self-consistent electronic minimizations were performed with ensemble density functional theory (EDFT) [51,73], where the Fermi-Dirac smearing scheme with an electronic temperature of 1000 K was applied. The electronic energies were converged to 1×10^{-5} eV, and the structural relaxations were conducted until the forces acting on each atom were below 0.05 eV Å^{-1} for the 96-atom simulation cell and 0.10 eV Å^{-1} for the 768-atom simulation cell.

The onsite Coulomb repulsion was accounted for by applying the Hubbard parameter U to favor localization of electronic states. A rotational invariant approach [51] was used with the U parameter chosen to be 5.0 eV. The choice of 5.0 eV was made with reference to its effect on calculated lattice parameter and band gap (Fig. 1 in the Supplemental Material [74]) and the range used in the computational literature [33,35,37,38]. Ramping U is less appropriate as it can affect the orbital orderings [50]. Using a U correction may give rise to metastable states, which have been studied with the occupation matrix control (OMC) scheme [32,75–77]. As we have introduced defects, applying OMC to the $5f$ states of plutonium would require sampling all possible states for mixed valence systems, which would be computationally unfeasible [77].

Optimization of the simulation cells containing defects was performed at constant volume using the ONETEP code, where a localization radius of 10.0 a_0 was used for the nonorthogonal generalized Wannier functions (NGWFs) of each valence state. The hydrogen 1s orbital was represented by one NGWF and four NGWFs were assigned to the oxygen valence states (one for the 2s orbital, three for the 2p orbitals). The plutonium valence states are represented by 17 NGWFs (one each for the 6s and 7s orbitals, three for the 6p orbitals, five for the 6d orbitals, and seven for the 5f orbitals).

The PuO_2 supercell was optimized with a periodic arrangement of collinear spin moments on the plutonium sites aligned along the (100) direction in an antiferromagnetic (AFM) arrangement. The AFM states in a one-dimensional collinear arrangement are assigned the label "1**k**." A longitudinal arrangement for the spins was chosen to give the 1**k**-AFM longitudinal magnetic ordering, based upon previous theoretical investigations [32,33,35,37,38,52,78]. These studies have found the AFM ground state to be energetically more favorable than the DM and FM ground states when OMC is not used [77]. The 1**k**-AFM longitudinal ordering

TABLE I. Bulk properties of PuO_2 calculated with plane-wave DFT and the comparison with experimental and computational literature.

Bulk properties	DFT+U	Computational literature	Experimental literature
Lattice constant a (Å)	5.48	5.47[a,b], 5.36[d], 5.45[e], 5.42[f], 5.46[g], 5.39[h], 5.47[i], 5.35[j]	5.40[k,m]
Band gap E_g (eV)	1.71	1.50[b], 2.20[c], 1.67[d], 2.00[e], 2.97[f], 1.60[g], 0.90[h], 1.70[i]	1.80[l,n], 2.80[o]
Magnetic moment μ_{mag} (μ_B)	4.34	4.17[b], 3.89[c], 3.80[f], 4.12[g], 3.72[h]	0.00[p,q,r,s]
Bulk modulus B_{VRH} (GPa)	187	197[b], 217[d], 199[e], 215[f], 198[g], 184[j]	
EOS bulk modulus B (GPa)	183	194[a], 199[c], 184[i]	178[n], 379[t]
EOS B'	4.88	4.50[a]	2.40[t]
Shear modulus G_{VRH} (GPa)	59	53[b], 126[d], 88[g], 81[j]	
Young's modulus E (GPa)	160	145[b], 231[g], 213[j]	
Poisson's ratio ν	0.36	0.38[b], 0.26[d], 0.31[g,j]	
C_{11} (GPa)	360	257[b], 348[d], 375[e], 369[g], 367[j]	
C_{12} (GPa)	101	168[b], 180[d], 111[e], 109[g], 92[j]	
C_{44} (GPa)	33	59[b], 166[d], 70[e], 71[g], 56[j]	
$C_{11} - C_{12}$ (GPa)	259	89[b], 168[d], 264[e], 260[g], 275[j]	
$C_{11} + 2C_{12}$ (GPa)	562	595[b], 708[d], 597[e], 587[g], 551[j]	

[a]Reference [33] (1**k**-AFM, $U = 5.00$ eV); [b]Reference [33] (1**k**-AFM, $U = 4.00$ eV); [c]Reference [32] (1**k**-AFM, $U = 4.00$ eV); [d]Reference [35] (1**k**-AFM, $U = 4.70$ eV); [e]Reference [78] (1**k**-AFM, $U = 4.00$ eV); [f]Reference [38] (Longitudinal 3**k**-AFM, $U = 6.00$ eV); [g]Reference [37] (1**k**-AFM, $U = 4.00$ eV); [h]Reference [77] (1**k**-AFM, $U = 4.50$ eV); [i]Reference [52] (1**k**-AFM, $U = 4.00$ eV); [j]Reference [82]; [k]Reference [23]; [l]Reference [24]; [m]Reference [83]; [n]Reference [25]; [o]Reference [26]; [p]Reference [28]; [q]Reference [29]; [r]Reference [30]; [s]Reference [31]; [t]Reference [84].

was chosen over the 3**k**-AFM noncollinear ordering as it is computationally less demanding to investigate.

B. Defect formation

Point defects were introduced into the stoichiometric structure of PuO_2, from the simulation cell initially optimized with CASTEP. The simulation cells were kept neutral, with no addition or removal of electrons. The defective structures were optimized at constant volume, using the lattice parameters of the relaxed, perfect cell. Larger supercells were created from the optimized 2×2×2 supercell of PuO_2. Fixed cell optimizations using ONETEP were performed on these larger supercells, in addition to the 96-atom supercell. Point defects were introduced into the resulting, stoichiometric structures and then optimized [79].

The energy required to form a point defect in perfectly crystalline PuO_2 is calculated according to the formula [80,81]

$$E_{\text{defect}}^{\text{form}} = E_{\text{defect}} - E_{\text{stoich}} - \sum_i n_i E_i, \tag{1}$$

where the total energy of the material containing the defect is denoted as E_{defect} and the total energy for the stoichiometric material is given by E_{stoich}. To form a defect in the crystal, n_i number of species of type i are either removed to form a vacancy ($n_i < 0$) or added to an interstitial site ($n_i > 0$). The energy for the addition or removal of each species is given E_i, where the energy for hydrogen or oxygen is calculated by optimizing a H_2 or O_2 molecule in the gas phase ($E = \frac{1}{2}E_{H_2}$ or $\frac{1}{2}E_{O_2}$). The energy for plutonium metal is calculated by optimizing the 32 atoms of bulk plutonium metal with an effective U of 5.0 eV applied. In general, the formation energy is positive, as it costs energy to create a defect.

We introduced Frenkel defects into the simulation cell by removing an atom from a lattice site and placing it in an interstitial position in the simulation cell. The defect formation energies of the Frenkel defects are presented per point defect,

$$E_{\text{Frenkel}}^{\text{form}} = \frac{E_{\text{defect}} - E_{\text{stoich}}}{2}. \tag{2}$$

The Schottky defect was created by the removal of a neutral, formula unit of PuO_2 from the initial cell. The formation energy for the Schottky defect is given per point defect,

$$E_{\text{Schottky}}^{\text{form}} = \frac{1}{3}\left(E_{\text{defect}} - E_{\text{stoich}} + \frac{E_{\text{stoich}}}{x}\right), \tag{3}$$

where x is the number of formula units in the supercell.

III. RESULTS AND DISCUSSION

A. Bulk properties of stoichiometric PuO_2

We initially used plane-wave DFT to calculate the bulk properties of stoichiometric PuO_2 from the 12-atom simulation cell and these properties are summarized in Table I. Our choice of GGA functional and value of U for the Hubbard correction both contribute to overestimating the lattice constant by 1.5% compared to experiment. However, our lattice parameters are broadly in line with the computational literature. A U correction of 5.0 eV creates a band gap of 1.71 eV, shown in Figs. 1 and 3 of the Supplemental Material [74]. Our calculated band gap is in good agreement with the computational studies by Zhang *et al.* [52] and Yang *et al.* [35], and is also close to the experimentally measured values by McNeilly *et al.* [24] and Idiri *et al.* [25]. The 1**k**-AFM longitudinal magnetic ordering gives a magnetic moment of $4.34\mu_B$ on each Pu^{4+} ion, which is comparable to other DFT studies. Experimental investigations have reported that PuO_2 has a DM ordering, however, we have the AFM ordering as DFT studies have found this to have a more stable ground state [32,33,35,37,38,52,78].

We determined the unique elastic constants of stoichiometric PuO_2 given in Table I, from which the mechanical properties are derived using the Voigt-Reuss-Hill (VRH)

approximation [85]. The mechanical stability of this cubic crystal was assessed by comparing the elastic constants with the Born-stability criteria [86] given by

$$\left\{\begin{matrix} C_{11} > 0; \quad C_{44} > 0 \\ C_{11} - C_{12} > 0 \\ C_{11} + 2C_{12} > 0 \end{matrix}\right\}. \tag{4}$$

Our calculated elastic constants satisfy the stability criteria and the C_{11} and C_{12} constants are in reasonable agreement to the computational literature values. Our value for C_{11} (360 GPa) falls within the range found in the literature (257–375 GPa) and is within 5% of the mean values reported; our value for C_{12} (101 GPa) is within the literature reported range (92–180 GPa) and is within 24% of the mean values reported. Our value for C_{44} (33 GPa) is lower than the literature reported range (56–166 GPa) by a significant margin (some 60% below the mean of values reported) although a wide range of values are reported and we are closer to the majority of values (56–71 GPa). We used the elastic constants to determine the bulk, shear, and Young's moduli as well as the Poisson's ratio. Our calculated G, E, and ν are in good agreement with the computational literature, falling within the range of reported values in each case.

The bulk modulus calculated from the Voigt-Reuss-Hill (VRH) approximation B_{VRH} is 187 GPa, which is lower than the range reported by the computational literature. We also calculated the bulk modulus by fitting the third-order Birch-Murnaghan equation of state (EOS), for different cell volumes shown in Fig. 2 of the Supplemental Material [74]. Fitting the cubic polynomial to the free energy-volume plot, the minimum bulk modulus at minimum volume B_0 is found to be 183 GPa or 1.14 eV/Å^3. The first derivative of B_0 with respect to pressure at constant temperature is the dimensionless parameter B_0', with a value of 4.88, which is typical for such material [9,33]. Comparisons to the experimentally determined bulk moduli are difficult, as we found only one report. Idiri *et al.* report 178 GPa [25] which is derived from a reevaluation of the data of Dancausse *et al.* [84]. The differences with our computational values are often attributed to temperature and volume effects [82], which are not accounted for by the approximations of the exchange-correlation functional in the DFT simulations.

B. Structure and electronic properties of point defects

1. Intrinsic point defects

Forming an oxygen vacancy in PuO_2 involves two excess electrons localizing onto two neighboring plutonium sites, reducing plutonium ions from Pu(IV) to Pu(III). This process is illustrated by the Kröger-Vink notation

$$\mathrm{O}_{\mathrm{O}}^{\times} + 2\mathrm{Pu}_{\mathrm{Pu}}^{\times} \rightarrow \mathrm{V}_{\mathrm{O}}^{\bullet\bullet} + 2\mathrm{Pu}_{\mathrm{Pu}}' + \tfrac{1}{2}\mathrm{O}_2(\mathrm{g}), \tag{5}$$

where $\mathrm{O}_{\mathrm{O}}^{\times}$ and $\mathrm{Pu}_{\mathrm{Pu}}^{\times}$ represent the oxygen and plutonium ions on their respective lattice sites. $\mathrm{V}_{\mathrm{O}}^{\bullet\bullet}$ corresponds to the doubly positively charged oxygen vacancy and the $\mathrm{Pu}_{\mathrm{Pu}}'$ corresponds to the single negatively charged plutonium Pu(III) ion. Figure 1(a) shows that the effective positive charge on the vacancy attracts the first nearest-neighbor oxygen ions, which move towards the vacant site from their lattice site. Mulliken population analysis shows that a stable ground state is found where two electrons localize onto one adjacent plutonium ion each.

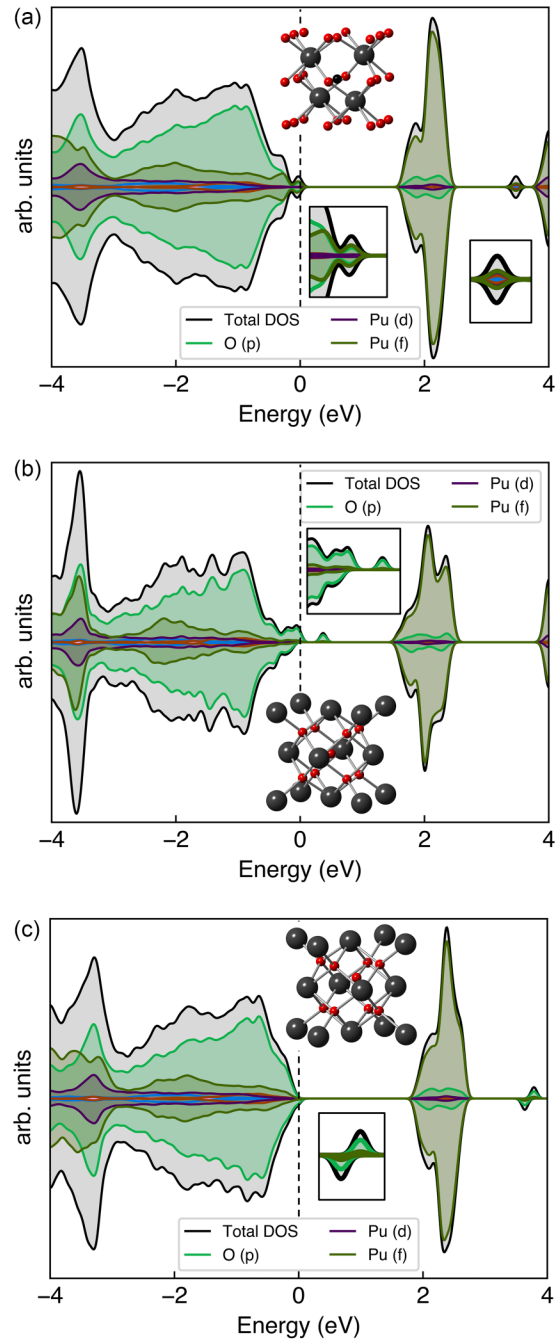

FIG. 1. Local structure around the (a) oxygen vacancy, (b) interstitial oxygen (octahedral), and (c) peroxide defects in PuO_2 and their respective PDOS plots for the 96-atom simulation cell from ONETEP. The oxygen atoms are given in red, plutonium atoms in gray, and the oxygen vacancy in black. The DOS plot is decomposed into the O-p (p), Pu-d (d), and Pu-f (f) states.

The projected density of states (PDOS) plotted with Sumo [87] in Fig. 1(a) shows that excess electrons occupy the empty $5f$ states on two neighboring plutonium ions. Additional peaks corresponding to the $5f$ state appear close to the oxygen $2p$ state dominated valence band and the conduction band

containing the plutonium $5f$ states. These peaks indicate the reduction of the neighboring Pu(IV) to Pu(III).

An oxygen was introduced into the octahedral interstitial site, which led to localized holes on the interstitial ion O_i' and neighboring oxygen ions $O_O^\bullet$:

$$O_O^x + \tfrac{1}{2}O_2(g) \rightarrow O_i' + O_O^\bullet. \quad (6)$$

Figure 1(b) shows that the oxygen atom placed in an octahedral interstitial lattice site produced additional peaks for the oxygen $2p$ state close to the valence band. The oxygen anion (O^-) remains in the octahedral interstitial site and we did not form the peroxide species with a neighboring lattice oxygen atom. Instead, the oxygen atoms in the lattice forming a cube around the octahedral site move away from the interstitial ion. To form the peroxide species (O_2^{2-}) shown in Fig. 1(c), the interstitial oxygen was placed approximately 1.0 Å from a lattice oxygen, along the ⟨111⟩ direction,

$$O_O^x + \tfrac{1}{2}O_2(g) \rightarrow (O_2)_O^x. \quad (7)$$

The lattice oxygen nearest to the interstitial oxygen moves from its lattice site towards the interstitial oxygen to form the peroxide species (O_2^{2-}). An O-O bond length of 1.46 Å was measured for the peroxide and the lattice O-Pu bond elongates from 2.38 to 2.62 Å. The PDOS for the peroxide species contains new peaks near the conduction band, belonging to the oxygen $2p$ states of the peroxide with no additional peaks in the band gap. These new oxygen $2p$ states are due to the antibonding orbitals generated by the formation of the peroxide species, as suggested by Keating *et al.* in their study of defects in ceria [88]. This is supported by the Mulliken charge analysis, where we found no localization of charge on the neighboring lattice sites.

Creating a plutonium vacancy removes four electrons from the lattice, which forms holes on the neighboring oxygen atoms,

$$Pu_{Pu}^x + 4O_O^x \rightarrow V_{Pu}'''' + 4O_O^\bullet + Pu(s), \quad (8)$$

where Fig. 2(a) shows that eight oxygen sites surrounding the plutonium vacancy move away from the effective negative charge of the vacant site. The PDOS for the plutonium vacancy defect indicates that holes are localized onto the oxygen $2p$ states, close to the valence band. Analysis of the Mulliken charge population suggests that four holes are delocalized across eight oxygen sites which form a cube around the vacancy.

Placing an interstitial plutonium ion in an octahedral interstitial site adds four extra electrons into the system. These additional electrons localize onto neighboring plutonium lattice sites, reducing them from Pu(IV) to Pu(III),

$$4Pu_{Pu}^x + Pu(s) \rightarrow 4Pu_{Pu}' + Pu_i^{\bullet\bullet\bullet\bullet}. \quad (9)$$

This introduction of the Pu(IV) also leads to the neighboring plutonium lattice sites relaxing away from the interstitial atom. Mulliken populations support the localization of four electrons across four adjacent plutonium atoms in the lattice. The PDOS shown in Fig. 2(b) contains several additional peaks in the band gap, where the shoulder peak of the valence band is the oxidized interstitial plutonium ion. The remaining peaks between the valence and conduction bands correspond

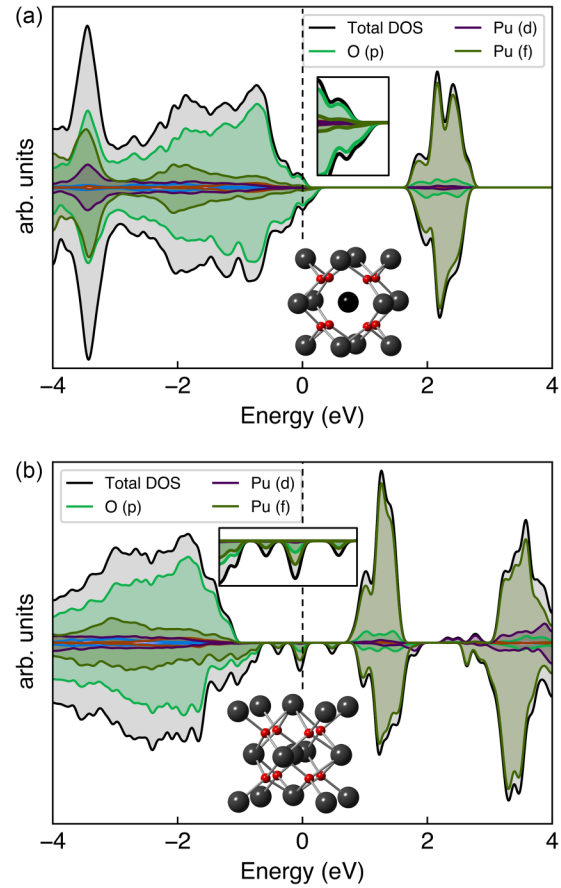

FIG. 2. Local structure around the (a) plutonium vacancy and (b) interstitial plutonium (octahedral) defects in PuO_2 and their respective PDOS plots for the 96-atom simulation cell from ONETEP. The oxygen atoms are given in red, plutonium atoms in gray, and the plutonium vacancy in black.

to the reduction of the neighboring plutonium lattice atoms from Pu(IV) to Pu(III).

For the oxygen substituted onto a plutonium lattice site, the holes localize across several oxygen sites,

$$Pu_{Pu}^x + 6O_O^x + \tfrac{1}{2}O_2(g) \rightarrow O_{Pu}'''''' + 6O_O^\bullet + Pu(s). \quad (10)$$

Figure 3(a) shows the oxygen ion (O^{2-}) substituted onto a plutonium lattice site (or placed on a vacant plutonium site V_{Pu}''''). The lattice oxygen sites which form a cube around the defect move away from the substituted plutonium site. This is akin to the behavior of the lattice when an oxygen ion is introduced into the octahedral interstitial site. Mulliken population analysis supports the delocalization of six holes across eight neighboring oxygen sites surrounding the defect. This is reflected in the PDOS which bears similar features to that of oxygen interstitial and plutonium vacancy PDOS. A peak close to the valence band is similar to that found in the PDOS for the creation of the plutonium vacancy, where holes form on the $2p$ states of the oxygen lattice sites. The other peak present in the band gap corresponds to the holes present on oxygen $2p$ states, as we found for the oxygen atom in the octahedral interstitial site.

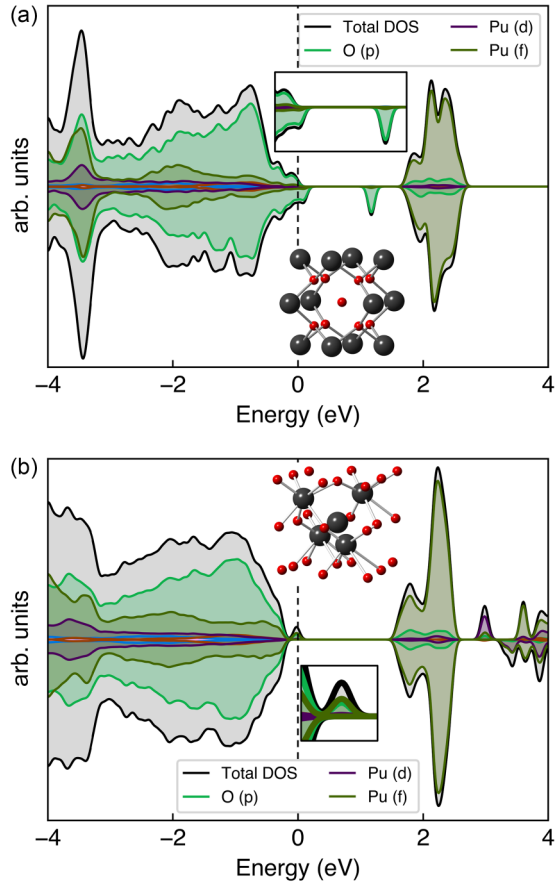

FIG. 3. Local structure around the defect for (a) oxygen substituted onto a plutonium site and (b) plutonium substituted onto oxygen site in PuO_2 and their respective PDOS plots for the 96-atom simulation cell from ONETEP. The oxygen atoms are given in red, and the plutonium atoms in gray.

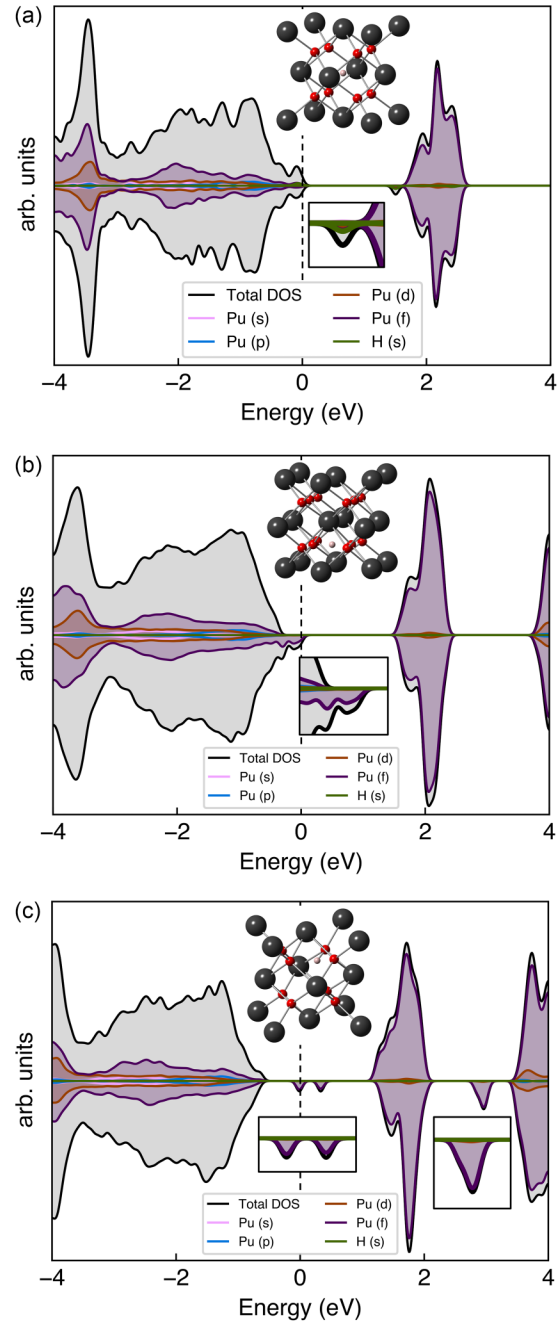

FIG. 4. Local structure around the interstitial hydrogen defect (a) in the octahedral site, (b) along the oxygen-edge site, and (c) hydroxyl species in PuO_2 and their respective PDOS plots for the 96-atom simulation cell from ONETEP. The oxygen atoms are given in red, plutonium atoms in gray, and the interstitial hydrogen atoms in pink.

Substitution of a plutonium atom onto an oxygen lattice site (or placed on a vacant oxygen site, $V_O^{\bullet\bullet}$), reduces several plutonium lattice sites from Pu(IV) to Pu(III),

$$5Pu_{Pu}^{x} + O_O^{x} + Pu(s) \rightarrow Pu_O^{\bullet\bullet\bullet\bullet\bullet} + 5Pu'_{Pu} + \tfrac{1}{2}O_2(g). \quad (11)$$

Examining the Mulliken charge on the plutonium sites, we found a total of five lattice sites which were reduced from Pu(IV) to Pu(III). The reduction of plutonium is indicated in the PDOS by the presence of a $5f$ peak close to the valence bad. The plutonium substitution on the oxygen lattice site distorts the PuO_2 as shown in Fig. 3(b). Oxygen lattice sites surrounding the defect are attracted and move towards the net positive charge. In contrast, the neighboring plutonium lattice sites move away from Pu(III) ion on the substituted oxygen lattice site.

2. *Hydrogen point defects*

Hydrogen was introduced into the octahedral interstitial lattice site as a radical,

$$\tfrac{1}{2}H_2(g) \rightarrow H_i^{\times}. \quad (12)$$

The hydrogen radical introduced into the octahdedral site is shown in Fig. 4(a). The PDOS for this defect does not exhibit any features consistent with other hydrogen species and therefore supports the identity as a radical hydrogen atom. Mulliken charge analysis on the neighboring oxygen and plutonium lattice sites also supports the presence of a hydrogen radical species in this interstitial position. There is also minimal distortion of the lattice atoms surrounding the radical hydrogen species from their preferred position.

The hydrogen cation species (H^+) was formed by placing the hydrogen atom midway between two oxygen lattice sites (oxygen edge),

$$Pu_{Pu}^{\times} + \tfrac{1}{2}H_2(g) \rightarrow H_i^{\bullet} + Pu_{Pu}^{\prime}. \quad (13)$$

The PDOS in Fig. 4(b) has an additional peak in the $5f$ state of plutonium near the valence band. This peak corresponds to the reduction of plutonium in the lattice from Pu(IV) to Pu(III). There is also an absence of additional peaks in the PDOS indicative of a hydrogen radical. The Mulliken charge analysis indicates that a single plutonium site neighboring the cationic hydrogen species is reduced from Pu(IV) to Pu(III). The H^+ ion attracts the adjacent oxygen lattice atoms, which shift off their respective sites towards it, separated equally from the the H^+ ion by 1.2 Å.

We were unable to form the hydroxyl (OH) species by placing the interstitial hydrogen along the center of the oxygen edge, where the separation between the hydrogen and lattice oxygen atoms was measured at 1.2 Å. This is much greater than the experimentally determined O-H bond length at 0.97 Å [89]. We did, however, form the OH species with the same approach to form the peroxide, where the interstitial hydrogen was placed approximately 1.0 Å from the lattice oxygen, along the ⟨111⟩ direction,

$$Pu_{Pu}^{\times} + O_O^x + \tfrac{1}{2}H_2(g) \rightarrow (OH)_O^{\bullet} + Pu_{Pu}^{\prime}. \quad (14)$$

Figure 4(c) shows the interstitial hydrogen atom bound to the oxygen atom on the corner of the oxygen lattice forming a cube. This lattice oxygen moves from its site towards the interstitial hydrogen to form the hydroxyl species. The bond length for the O-H bond was measured at 0.97 Å (96-atom cell) and 0.99 Å (768-atom cell), and the lattice O-Pu bond extends from 2.38 to 2.56 Å (96-atom cell) and 2.49 Å (768-atom cell) in length. Similar to the hydrogen along the oxygen edge, the Mulliken charge analysis suggests the reduction of a neighboring plutonium lattice site. The PDOS includes additional $5f$ peaks, which correspond to the reduction of plutonium in the lattice.

Hydrogen was substituted onto an oxygen lattice site, which formed a hydride (H^-) and reduced a neighboring plutonium lattice site from Pu(IV) to Pu(III),

$$Pu_{Pu}^{\times} + O_O^x + \tfrac{1}{2}H_2(g) \rightarrow H_O^{\bullet} + Pu_{Pu}^{\prime} + \tfrac{1}{2}O_2(g). \quad (15)$$

Figure 5(a) shows the hydrogen substituted onto an oxygen lattice site. The hydride remains on the oxygen lattice site with a small shift from the neighboring lattice oxygen atoms towards it (it has a net positive charge compared to the original oxygen anion). The PDOS shows a plutonium $5f$ peak close to the valence band which indicates the reduction of a plutonium lattice site. This feature is similar to that found for the reduction of plutonium lattice sites on the creation of the oxygen vacancy. The Mulliken population analysis supports the reduction of one neighboring plutonium site from Pu(IV) to Pu(III).

Substituting hydrogen onto a plutonium lattice site localizes holes across several oxygen sites,

$$Pu_{Pu}^{\times} + 5O_O^x + \tfrac{1}{2}H_2(g) \rightarrow H_{Pu}^{\prime\prime\prime\prime\prime} + 5O_O^{\bullet} + Pu(s). \quad (16)$$

The Mulliken population analysis suggests that this substitution leaves five holes localized across eight oxygen lattice sites. This is demonstrated in Fig. 5(b) with additional peaks in PDOS for the oxygen $2p$ state close to the valence band, indicating the localization of holes on oxygen lattice sites. This feature is comparable to the PDOS for the creation of plutonium vacancy, where we also found the delocalization of holes over eight oxygen lattice sites, which move away from their lattice sites. The PDOS also contains a peak for the hydrogen $1s$ state in the band gap, which suggests the formation of a hydride species on the plutonium lattice site.

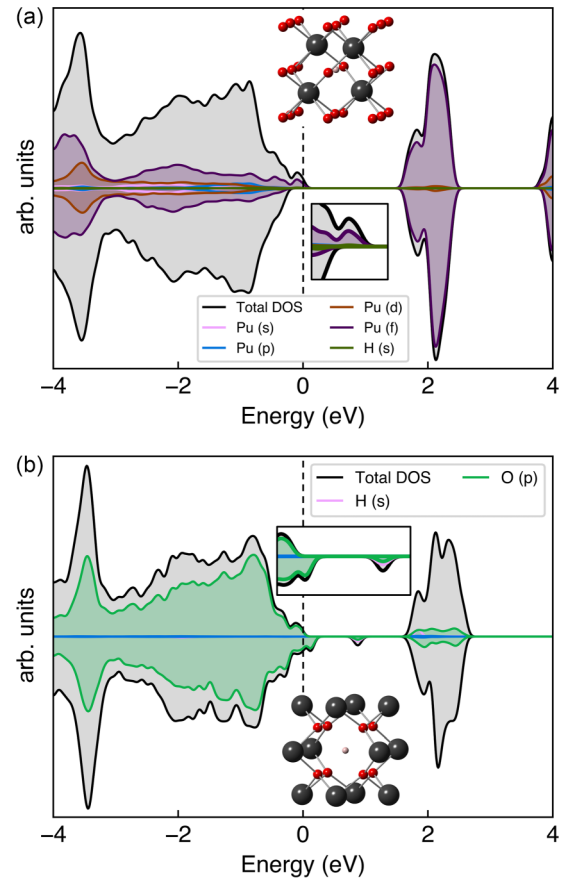

FIG. 5. Local structure around the hydrogen substitution defect on the (a) oxygen site and (b) plutonium site in PuO_2 and their respective PDOS plots for the 96-atom simulation cell from ONETEP. The oxygen atoms are given in red, plutonium atoms in gray, and the hydrogen atom in pink.

C. Energetics of defects

1. Intrinsic point defect formation

The intrinsic point defect formation energies in PuO_2 were determined at different simulation sizes with ONETEP. Table II lists our intrinsic defect energies, which are presented alongside the available defect energies from computational literature. Our defect energies are presented under stoichiometric conditions, without considering the dependence of the chemical potential of plutonium or oxygen on the partial pressure of oxygen.

Creating an oxygen vacancy removes 1.6% of oxygen atoms (PuO_{2-x} where $x = 0.03$) in the 96-atom supercell, and

TABLE II. Formation energies for the oxygen and plutonium point defects calculated using DFT+U for stoichiometric PuO_2 and comparison to the computational literature.

	ONETEP (eV)		Computational literature (eV)	
Defect	96 atom	768 atom	96 atom	324 atom
$V_O^{\bullet\bullet}$	2.35	3.13	5.30[a,b], 4.89[c], 3.19[d], 3.41[e]	3.40[d]
O_i' (octahedral)	2.07	2.11	0.10[a,b], 1.98[d], 0.78[e]	2.12[d]
$(O_2)_O^{\times}$ (peroxide)	1.57	2.67		
O_{Pu}''''''	14.03	15.01	2.08[f], 12.11[g]	
V_{Pu}''''	12.53	13.16	9.20[a,b], 5.14[c], 14.00[d], -1.09[f], 8.94[g]	14.03[d]
$Pu_i^{\bullet\bullet\bullet\bullet}$ (octahedral)	1.59	1.12	4.90[a,b], 11.18[f], 1.15[g]	
$Pu_O^{\bullet\bullet\bullet\bullet\bullet}$	4.22	4.43	22.90[f], 12.88[g]	

[a]Reference [90]; [b]Reference [55]; [c]Reference [56] (1**k**-AFM, $U = 3.0$ eV); [d]Reference [12] (1**k**-AFM, $U = 4.0$ eV); [e]Reference [91] ($U = 4.0$ eV); [f]Reference [91] (Oxygen rich, $U = 4.0$ eV); [g]Reference [91] (Oxygen poor, $U = 4.0$ eV).

increasing the simulation size to 768 atoms dilutes the concentration to 0.2% (where $x = 0.004$). Our calculated formation energies for the oxygen vacancy are lower than that found in previous theoretical studies [12,56,90]. At the 768-atom simulation cell size, the oxygen vacancy formation energy is comparable to that of energies reported by Holby *et al.* [12]. Consistent with that study, we also find increasing energies for the oxygen vacancy in the larger simulation cell. The nearest-neighbor lattice oxygen atoms relax from their equilibrium positions by up to 0.29 and 0.24 Å for 96- and 768-atom simulation cells, respectively.

Creating a plutonium vacancy removes 3.1% of plutonium atoms in the 96-atom supercell, and 0.4% in the 768-simulation cell. A broader range of defect energies has been reported for the plutonium vacancy. Our plutonium vacancy energies are in closest agreement to those calculated by Holby *et al.* [12]. A negligible increase in relaxation of the nearest-neighbor oxygen atoms away from their sites was measured, from up to 0.22 Å in the 96-atom cell to 0.23 Å in the 768-atom cell. As with the oxygen vacancy defect, the oxygen lattice displacement is most pronounced for the first-nearest neighbors to the plutonium vacancy. The disruption to the nearest-neighbor plutonium lattice ions from their equilibrium position is minimal.

We calculated similar defect formation energies for the interstitial oxygen in the octahedral site, at both 96- and 768-atom supercell sizes. Our oxygen interstitial defect energies are comparable to those given by Holby *et al.* [12]. The interstitial oxygen remains in the octahedral site with the nearest-neighbor oxygen ions moving away from the defect by up to 0.14 Å from their sites. Placing the interstitial oxygen at 1.0 Å from an lattice oxygen site, along the ⟨111⟩ direction we formed peroxide species. We measured the O-O bond length for the peroxide at 1.46 Å at both supercell sizes, which is close to the reported 1.45 Å bond length [92].

For the plutonium interstitial placed in the octahedral interstitial site, the defect energies we have calculated are larger for the 96-atom supercell and decrease significantly for the larger (768-atom) simulation cell size. Our plutonium interstitial defect energies are considerably lower than those reported by reported by Freyss *et al.* [55,90], but close to the energy calculated by Singh *et al.* under oxygen-poor conditions [91]. The nearest-neighbor plutonium sites relax away from the interstitial defect by as much as 0.28 Å in the 96-atom simulation cell, and 0.37 Å in the 768-atom cell. A greater distortion of the lattice around the interstitial plutonium may be responsible for the lower defect energy in the 768-atom supercell, as a larger simulation cell can more effectively accommodate the changes in the lattice around the defect site.

Substituting oxygen on a plutonium lattice site, the oxygen was found to remain on the plutonium lattice site. The nearest-neighbor lattice oxygen ions move away from their lattice sites by up to 0.22 Å. Oxygen substitution at a plutonium lattice site is calculated to be the least energetically favorable intrinsic defect, where our defect formation energy is closer to that calculated by Singh *et al.* under oxygen-poor conditions [91]. Our results find that the plutonium on an oxygen site is more energetically favorable (4.2–4.4 eV) than the oxygen on a plutonium site (14–15 eV). In contrast, Singh *et al.* [91] found that the plutonium on an oxygen site is less energetically favorable than the oxygen on a plutonium site (whether for oxygen-rich or oxygen-poor PuO_2). For plutonium placed on the oxygen site, the nearest-neighbor oxygen ions to move towards the plutonium placed on the oxygen site by up to 0.51 Å in the 96-atom cell and up to 0.48 Å in the 768-atom cell. In this case the separation of plutonium to the lattice oxygen is measured at 2.40 Å (96 atom) and 2.45 Å (768 atom).

2. *Frenkel defect formation*

The oxygen Frenkel (OF) defect was created by creating a vacancy on an oxygen lattice site and placing an oxygen in an octahedral interstitial position. Figure 9 in the Supplemental Material [74] illustrates the position of the interstitial oxygen atom placed along the ⟨111⟩ direction (purple) from the vacant site (black). The oxygen Frenkel defect formation process is represented by the Kröger-Vink notation

$$O_O^x \rightarrow V_O^{\bullet\bullet} + O_i''. \tag{17}$$

The plutonium Frenkel (PuF) defect was created in a the same manner as the oxygen Frenkel defect. Figure 10 in the Supplemental Material [74] shows the plutonium vacancy (black) in the simulation cell and the interstitial plutonium atom placed along the ⟨111⟩ direction (purple). The plutonium Frenkel defect formation process may be represented by

$$Pu_{Pu}^x \rightarrow V_{Pu}'''' + Pu_i^{\bullet\bullet\bullet\bullet}. \tag{18}$$

TABLE III. O Frenkel (OF) and Pu Frenkel (PuF) defect formation energies at infinite dilution and along the ⟨111⟩ direction and comparison to the computational literature.

	ONETEP (eV)		Computational literature (eV)
Defect	96 atom	768 atom	96 atom
OF_∞	2.21	2.62	2.65[a,b], 2.21[c], 4.89[d], 1.74[e], 2.29[f], 2.45[g], 2.10[h]
OF⟨111⟩	1.60	2.29	2.24[f]
PuF_∞	7.06	7.14	7.05[a,b], 9.89[d], 7.60[e], 5.01[f], 6.93[g], 5.05[h]
PuF⟨111⟩	4.99	6.65	10.04[h]

[a]Reference [90]; [b]Reference [55]; [c]Reference [95] (1**k**-AFM); [d]Reference [56] (1**k**-AFM, $U = 3.0$ eV); [e]Reference [57] (1**k**-AFM, $U = 4.0$ eV); [f]Reference [96] ($U = 4.0$ eV); [g]Reference [97] (Longitudinal 3**k**-AFM, $U = 7.0$ eV); [h]Reference [91] ($U = 4.0$ eV).

The 96-atom supercell limits the separation between vacant and interstitial sites for the Frenkel defect. Expanding the optimized simulation cell to 768 atoms in size allowed the placement of the interstitial atom further from the vacancy. Increasing the separation between the interstitial atom and the vacancy serves to reduce the interaction between the two sites within the cell. To avoid recombination, we find that placing the interstitial oxygen atom at least one interstitial site away from the vacancy is sufficient separation [79,93,94].

Table III lists the oxygen and plutonium Frenkel defect formation energies along the ⟨111⟩ direction in the simulation cell. The Frenkel defect energies have also been calculated at infinite dilution and are presented alongside the computational literature. For the 96-atom cell, the interstitial oxygen and plutonium atoms were placed at 11.9 and 4.8 Å, respectively, from the vacant site. This separation was increased in the 768-atom supercell to 21.4 Å for oxygen and 14.2 Å plutonium Frenkel defects to minimize the interaction between the vacancy and interstitial sites. Our previous investigation of Frenkel defects in ceria [79] suggests that the increased separation along the ⟨111⟩ direction in the 768-atom simulation cell is sufficient.

At infinite dilution, our calculated oxygen Frenkel defect energies are close to the energies reported by several other computational studies [55,90,91,96,97]. When the vacancy and interstitial are introduced along the ⟨111⟩ direction within the same simulation cell, the defect energies are lower than at infinite dilution. The lower defect energies are a consequence of the electrostatic interaction between the oppositely charged oxygen vacancy and interstitial sites. In the 96-atom supercell, the oxygen Frenkel energy is lower when compared to the 768-atom cell. This is because the separation between the interstitial ion oxygen and the vacancy in the periodic image is reduced to 7.1 Å in the 96-atom cell. Whereas, in the 768 simulation cell, the interstitial oxygen is 16.6 Å apart from the vacancy in the periodic image. Placing the interstitial ion further apart in the larger simulation cell serves to increase the oxygen Frenkel energy, as stabilizing interaction between the vacancy and interstitial oxygen are reduced. We found our oxygen Frenkel energies to be lower than that reported by Nakamura *et al.* [96], as they may have placed the vacancy and interstitial oxygen in different positions.

For the plutonium Frenkel defects at infinite dilution, the defect energies are close between the 96- and 768-atom simulation cells. We also have good agreement between our defect energies and several computational studies [55,57,90,97]. As with the oxygen Frenkel defect, introducing the plutonium vacancy and interstitial along the ⟨111⟩ direction within the same simulation cell leads to smaller defect formation energies. Our defect formation energy is approximately half that of the only other available calculation by Singh *et al.* along the same direction [91]. In the 96-atom supercell, the plutonium interstitial is 14.2 Å from the nearest periodic image of the vacant site. This separation increases to 23.7 Å in the 768-atom cell, which weakens the stabilizing electrostatic interaction between the interstitial plutonium and the vacancy. Hence, a larger plutonium Frenkel defect formation energy was calculated for the 768-atom simulation cell.

3. *Schottky defect formation*

The Schottky defects in Fig. 11 of the Supplemental Material [74] are introduced by removing one formula unit of PuO_2, which leaves one plutonium and two oxygen vacancies. Three Schottky defect configurations are possible depending on the positions of the oxygen vacancies around the plutonium vacancy. Keeping the position of one oxygen vacancy fixed, we can create the second oxygen vacancy along the ⟨100⟩, ⟨110⟩, and ⟨111⟩ directions. The Schottky formation process is summarized by

$$\mathrm{Pu}_{\mathrm{Pu}}^{\mathrm{x}} + 2\mathrm{O}_{\mathrm{O}}^{\mathrm{x}} \rightarrow \mathrm{V}_{\mathrm{Pu}}^{''''} + 2\mathrm{V}_{\mathrm{O}}^{\bullet\bullet}, \tag{19}$$

where removing the formula unit of PuO_2 leaves oppositely charged vacancies on the plutonium and oxygen lattice sites.

Table IV lists the calculated defect formation energies for the bound Schottky defects placed along ⟨100⟩, ⟨110⟩, and ⟨111⟩ directions in the simulation cell. The Schottky defect energies have also been calculated at infinite dilution and are presented with the computational literature. At infinite dilution, our calculated Schottky energy for the 96-atom simulation cell is closest to the energies reported by Freyss *et al.* [55,90] and comparable to several other studies [57,95,97]. For the 768-atom simulation cell size, we found an increase in the Schottky energy, however, our calculated energy is still within the range of energies reported for the 96-atom supercell in the literature.

In the 96-atom supercell, the Schottky defect along the ⟨110⟩ direction is predicted to be the most favorable. The ⟨111⟩ direction becomes the most favorable at the 768 simulation size, whereas the ⟨100⟩ direction remains the least stable Schottky defect for both supercell sizes. We have reported identical trends for the bound Schottky defects in ceria [79], where a simulation cell with more than 96 atoms changes the energetic ordering. The calculations by Singh *et al.* suggest

TABLE IV. Schottky (S) defect formation energies along the ⟨100⟩, ⟨110⟩, and ⟨111⟩ directions and comparison to the computational literature.

	ONETEP (eV)		Computational literature (eV)
Defect	96 atom	768 atom	96 atom
S_∞	2.89	3.58	3.03[a,b], 2.37[c], 4.97[d], 2.50[e], 2.03[f], 2.55[g], 1.91[h], 5.25[i]
$S\langle 100\rangle$	1.72	2.01	1.38[j]
$S\langle 110\rangle$	1.53	1.72	1.21[j]
$S\langle 111\rangle$	1.61	1.60	1.20[j]

[a]Reference [90]; [b]Reference [55]; [c]Reference [95] (1**k**-AFM); [d]Reference [56] (1**k**-AFM, $U = 3.0$ eV); [e]Reference [57] (1**k**-AFM, $U = 4.0$ eV); [f]Reference [96] ($U = 4.0$ eV); [g]Reference [97] (Longitudinal 3**k**-AFM, $U = 7.0$ eV); [h]Reference [91] (Oxygen rich, $U = 4.0$ eV); [i]Reference [91] (Oxygen poor, $U = 4.0$ eV); [j]Reference [91] ($U = 4.0$ eV).

that the $S\langle 110\rangle$ and $S\langle 111\rangle$ energies are much closer in energy than we have found in the 96-atom simulation cell [91]. Across all three directions for the bound Schottky defect, we found our energies were lower than at infinite dilution for both simulation cell sizes. At infinite dilution, the charged vacancies interact with neighboring periodic images, whereas in the bound Schottky defect, a charge neutral molecular unit of PuO_2 was removed.

The bent geometry of the Schottky defect along the ⟨100⟩ and ⟨110⟩ directions produces an effective dipole. Where there is no alignment of the positive charge on the plutonium cation with that of the negative charge on the each of the oxygen anions. The linear geometry of the Schottky defect in ⟨111⟩ direction leads to no dipole moment. In the work by Burr *et al.* they conclude that the electrostatic interactions alone cannot account for the finite-size effects [98]. Artificial restoring forces from the periodic boundary conditions (PBC) suppress the atomic relaxation around the defect in the 96-atom cell. This raises the energy of Schottky defect along the ⟨111⟩ direction compared to the ⟨110⟩ direction.

4. Hydrogen point defect formation

The hydrogen point defect formation energies in PuO_2 under stoichiometric conditions were calculated at different simulation sizes with ONETEP. Table V lists our hydrogen defect energies along with the defect energies from computational literature. Figure 12 in the Supplemental Material [74] shows the positions of each hydrogen point defect.

TABLE V. Formation energies for the hydrogen point defects calculated using DFT+U for stoichiometric PuO_2 and comparison to the computational literature.

	ONETEP (eV)		Computational literature (eV)
Defect	96 atom	768 atom	96 atom
$H_i^\times$ (octahedral)	2.43	3.38	2.32[a], 2.24[b], 2.30[c], 1.49[d]
$H_i^\bullet$ (oxygen edge)	1.14	1.40	0.54[b], 1.01[c]
$(OH)_O^\bullet$ (hydroxyl)	1.17	1.56	0.35[a], 0.97[c], 0.64[d,e]
$H_O^\bullet$	2.69	3.81	
$H_{Pu}^{////}$	13.71	15.54	

[a]Reference [11] (1**k**-AFM, $U = 4.0$ eV).
[b]Reference [12] (1**k**-AFM, $U = 4.0$ eV).
[c]Reference [13] (1**k**-AFM, $U = 4.0$ eV).
[d]Reference [14] (Longitudinal 3**k**-AFM, $U = 6.0$ eV).
[e]Reference [14] (Longitudinal 1**k**-AFM).

Interstitial hydrogen was initially introduced in the octahedral interstitial site, where we found an increase in defect energy between the 96- and 768-atom simulation cells. At the 96-atom supercell, our calculated defect energies are comparable to those reported in the studies by Ao *et al.* [11] and Holby *et al.* [13]. Minimal changes to the structure of the PuO_2 lattice were found around the interstitial hydrogen radical defect at both supercell sizes. Inserting the hydrogen into the middle of the oxygen edge, the cationic hydrogen species (H^+) attracts the neighboring oxygen lattice ions towards it. Displacement of the nearest lattice oxygen ions towards the hydrogen defect were measured up to 0.16 and 0.20 Å in the 96- and 768-atom simulation cell, respectively. The separation between the hydrogen and the lattice oxygen ions was measured as 1.22 Å (96 atom) and 1.16 Å (768 atom), which is greater than the 0.97 Å bond length for hydroxyl species [89].

The hydroxyl species was formed in a similar way to the peroxide species, where the hydrogen was placed approximately 1.0 Å from a lattice oxygen, along the ⟨111⟩ direction. The oxygen is displaced of its lattice site towards the interstitial hydrogen to form the O-H bond, which we measured at 0.97 and 0.99 Å in the 96- and 768-atom simulation cell, respectively. Our calculated defect energy is closer to that reported in the study of Zhang *et al.* [13], where they also measure an O-H bond length of 0.99 Å. A range of formation energies at increasing O-H bond lengths are reported in the study by Ao *et al.* [11], where they show that the longer O-H bond lengths (and hence a weaker bond) contribute to higher defect formation energies. A minimum for the defect formation energy in their study was found in the region of distances 0.90 to 1.0 Å at 0.35 eV.

On the oxygen lattice site, the hydrogen exists as a hydride (H^-) ion. We measured a displacement of the nearest-neighbor oxygen sites towards the hydride of 0.09 and 0.06 Å in the 96- and 768-atom cell, respectively. Our calculation suggests that substitution of oxygen ion by hydrogen is more favorable than substituting a plutonium ion with hydrogen. The substitution of a lattice oxygen with hydrogen has comparable formation energies to placing a hydrogen in the octahedral site. On the plutonium lattice site the hydrogen also exists as a hydride (H^-) ion. Substituting hydrogen onto a plutonium lattice site was found to be the least stable

TABLE VI. Comparison of the hydrogen substitution formation energies which are recalculated according to the methodology detailed by Holby *et al.* [12] in Eq. (20).

	ONETEP (eV)		Computational literature (eV)
Defect	96 atom	768 atom	96 atom
$H_O^{\bullet}$	0.34	0.69	0.14[a]
$H_{Pu}^{////}$	1.18	2.38	−2.62*[a]

[a]Reference [12] (1**k**-AFM, $U = 4.0$ eV).
*Formation of the hydroxyl (OH) species.

extrinsic defect, becoming more unfavorable in the 768-atom cell. The hydride remains in the substituted plutonium lattice site, with the nearest-neighbor oxygen ions moving off their lattice sites by 0.14 and 0.10 Å in the 96- and 768-atom cell, respectively.

The work of Holby *et al.* includes the substitution of hydrogen onto the oxygen and plutonium lattice sites [12]. In their study, the hydrogen substitution energies which are summarized in Table VI are calculated from a substoichiometric reference. For validation of our results against Holby *et al.*, we have recalculated our hydrogen substitution energies, using their methodology detailed by Holby *et al.* [12],

$$E_{\text{defect}}^{\text{form}} = E_{\text{defect}} - E_{\text{substoich}} - E_i, \tag{20}$$

where E_{defect} is the energy of the relaxed system with the impurity substituted onto an oxygen or plutonium site. The energy of the relaxed system containing an oxygen or a plutonium vacancy is given by $E_{\text{substoich}}$, and E_i is the energy of the introduced hydrogen.

Our recalculated substitution energies maintain the same energetic ordering as found using the stoichiometric reference. We found the defect energies for the substitution of H^- ion onto the oxygen site to be larger than the literature for the 96-atom simulation cell. The formation energies for both substitution mechanisms approximately double at the more dilute concentration in the 768-atom cell between the two methodologies. The simulation performed by Holby *et al.* for the hydrogen substitution onto the plutonium lattice site is reported to lead to the formation of the hydroxyl species [12]. They report that the hydrogen moves from the plutonium site towards an oxygen lattice site by 1.23 Å, to form the O-H bond with length of 0.98 Å. We were only able to form this hydroxyl species by displacing the hydrogen approximately 1.3 Å from the plutonium vacancy, before performing the geometry relaxation.

5. Hydrogen transport

The long-term goal of our studies of the defect chemistry of PuO_2 is to understand the influence of radiation damage and defects on the hydrogen permeability through the PuO_2 system. In this regard, it is worthwhile comparing our data with the computational literature, particularly focusing on hydrogen transport mechanisms in PuO_2, to see to what extent our results support other work.

Ao *et al.* [11] calculated the formation energy of a hydrogen moving from the site we label as hydroxyl towards the octahedral interstitial site. The authors do not propose this as a hydrogen diffusion pathway but with reference to their data we can calculate an activation energy of 1.97 eV for this pathway [from a simple difference between 0.35 eV (hydroxyl) to 2.32 eV (octahedral)]. Zhang *et al.* [13] subsequently examined an alternative pathway using the NEB method: that of the hydroxyl in one position of the oxygen cube (pointing to the octahedral interstitial) moving to a neighboring oxygen in the same oxygen cube pointing to the same interstitial, and then subsequently rotating around the oxygen to point to an adjacent octahedral interstitial. Zhang *et al.* report that this complete route has an activation energy of only 0.13 eV. The authors do not report NEB results for the hydroxyl to octahedral interstitial pathway but if we assume it can be calculated from the difference in energy between the two states, then it would, from their calculations, range 1.17–1.33 eV. The work of Zhang *et al.* would therefore suggest that the hydroxyl to hydroxyl pathway is more likely than the hydroxyl to octahedral pathway.

Goldman *et al.* [14] consider these same mechanistic pathways using NEB methods and find that the hydroxyl to hydroxyl pathway was in the range 0.15–1.17 eV for the first part (hydroxyl to oxygen edge to hydroxyl in the same oxygen cube) and 0.06–0.36 eV for the second part (hydroxyl in one oxygen cube rotating to hydroxyl in an adjacent oxygen cube). For the hydroxyl to octahedral pathway Goldman *et al.* report an activation energy of 0.27–0.36 eV, i.e., possibly lower than the hydroxyl to hydroxyl pathway and in contrast to Zhang *et al.* We have not yet progressed to NEB methods but if we take the gross assumption that the activation energies for these pathways are determined by the relative energies of the hydroxyl, octahedral, and oxygen-edge positions, then our ONETEP calculations suggest an activation energy of 1.26–1.82 eV for the hydroxyl to octahedral interstitial pathway, and 0.03–0.16 eV for the hydroxyl to hydroxyl pathway. Thus, our results are more in line with those of Zhang *et al.*, although this may be modified in light of future NEB calculations. One final point of note is that, in our work, the oxygen-edge position was always lower in energy than the hydroxyl position. This is in contrast to the work of Zhang *et al.* [13], although the magnitude of the difference was similar. This perhaps demonstrates that these positions are fairly close in energy with the difference perhaps being of lower magnitude than the accuracy of the calculations. These results are compiled in Table VII.

The energetics of such pathways might be modified by radiation damage in complex ways. First, the radiation damage can introduce defects that can act as stable sites for hydrogen (so stable that the defect may act as a sink and not release the hydrogen) our results so far do not identify this for simple point defects. Second, the radiation damage may introduce or remove atoms that are critical to the transport pathway. For example, we know that the majority of introduced defects are anionic Frenkel pairs where an oxygen will be moved from an oxygen cube and inserted into an interstitial (quite possibly an octahedral interstitial site). This may influence any potential pathways for hydrogen migration.

In the case of the hydroxyl-hydroxyl pathway the loss of an oxygen on the cube would appear to make the route more difficult as we show that the hydrogen on the oxygen vacancy is of higher energy (we calculate 2.69 and 3.81 eV). We have

TABLE VII. Hydrogen migration pathway energy calculated for the hydroxyl to hydroxyl species and the hydroxyl species to the interstitial (octahedral) site.

	ONETEP (eV)		Computational literature (eV)
Pathway	96 atom	768 atom	96 atom
Hydroxyl to hydroxyl	0.03*	0.16*	0.13[a], 0.15–1.17 followed by 0.06–0.36[b]
Hydroxyl to interstitial (octahedral)	1.26*	1.82*	1.97[c], 1.17–1.33*[a], 0.27–0.36[b]

[a]Reference [13] (1**k**-AFM, $U = 4.0$ eV).
[b]Reference [14] (DFT and DFTB).
[c]Reference [11] (1**k**-AFM, $U = 4.0$ eV).
*Calculated with only the difference between hydroxyl, oxygen-edge, and octahedral interstitial positions.

not yet calculated the energetics of hydroxyl to octahedral interstitial pathway where the interstitial is occupied by oxygen; one might assume this would be a more complicated pathway. Cationic Frenkel pairs where a plutonium atom is displaced to an octahedral interstitial site would perhaps have less of an effect on the hydroxyl to hydroxyl pathway, but may have a more dramatic effect on the hydroxyl to octahedral interstitial pathway.

The introduction of defects may also have complicated influences on "nearby" transport routes, and these are the subject of future studies. For example, one could imagine that removal of an oxygen from an oxygen cube would alter the energetics of how hydrogen could migrate across the remainder of the cube. Similarly, we have shown here that inserting an oxygen into the octahedral interstitial influences the oxygens in the surrounding cube to move further away. The presence of the interstitial and the new positions of the oxygen cube anions would probably influence the formation energy of any hydroxyl pointing towards an interstitial oxygen.

IV. CONCLUSIONS

Using large-scale DFT as implemented in the ONETEP code, we have examined a range of point defects, Frenkel pairs, Schottky defects, and hydrogen-related defects in the PuO_2 system in supercells containing 96 and 768 atoms.

For the point defects we have examined, note the following: 1. insertion of plutonium and oxygen into the octahedral interstitial; 2. vacancies of both oxygen and plutonium; 3. insertion of plutonium and oxygen into vacancies of oxygen and plutonium; 4. generation of a peroxide species. We find that the oxygen octahedral interstitial is, in general, the lowest formation energy point defect related to oxygen (2.07–2.11 eV), closely followed by the oxygen vacancy defect (2.35–3.13 eV). This is in agreement with the literature. We were also able to identify a stable peroxide species (1.57–2.67 eV) by placing an interstitial oxygen at 1.0 Å from a lattice oxygen site on the ⟨111⟩ direction. This defect has an O-O distance of 1.46 Å and has not been reported before. Both the plutonium vacancy and the oxygen inserted into the plutonium vacancy are found to be high in energy (12–15 eV). Finally, of note, we calculate the energy of a plutonium inserted into the octahedral interstitial site to be in the range of 1.12–1.59 eV and lower than reported in the literature (4.90 eV) [55,90].

Our calculations of Frenkel pair formation energies compare well with the literature, both at infinite dilution (OF_∞ at 2.21–2.62 eV, PuF_∞ at 7.06–7.14 eV) and along the ⟨111⟩ direction when placed in the same supercell (OF⟨111⟩ at 1.60–2.29 eV, PuF⟨111⟩ at 4.99–6.65 eV). We have also calculated the plutonium Frenkel pair along the ⟨111⟩ direction and we believe this is the first calculation of this type of defect in PuO_2: we report that the plutonium Frenkel pair defect has a formation energy of 4.99 eV in the 96-atom supercell and 6.65 eV in the 768-atom supercell.

Similarly, our Schottky defect formation energies at infinite dilution (2.89–3.58 eV) compare well to literature values. In addition to this, we examined Schottky defects in ⟨100⟩, ⟨110⟩, and ⟨111⟩ directions, where we find in each case the Schottky defect formation energies simulated in a single supercell (1.53–2.01 eV) are lower than those calculated at infinite dilution. In general, these energies were lower for the 96-atom supercell as compared to the 768-atom supercell. We find that the energetic ordering trends of these Schottky defects are identical to our results from the isostructural CeO_2 system and vary with supercell size [79].

Finally, we examined a number of likely hydrogen sites in the PuO_2 lattice: octahedral interstitial, oxygen edge, hydroxyl, oxygen vacancy, and plutonium vacancy. The hydrogen at the oxygen and plutonium vacancies is relatively high in energy (2.69–3.81 eV and 13.71–15.54 eV, respectively); these have not been reported before. We also find that the hydrogen exists as a radical at the octahedral interstitial site (2.43–3.38 eV) and that this is somewhat higher formation energy than other studies find [11–14]. Hydrogen at the oxygen edge (as a H^+ cation) and at the oxygen cube corner (as a hydroxyl) are both lower in energy (1.14–1.40 eV and 1.17–1.56 eV, respectively) as composed to hydrogen in the octahedral interstitial site (2.43–3.38 eV), but again higher than found by other studies [11–14]. It is noteworthy that our finding of a formation energy difference between the octahedral interstitial hydrogen and the hydrogen at oxygen edge/hydroxyl of 1.3–2.0 eV compares well to a similar value from the literature of 1.3–1.4 eV (calculated from a mean of literature values). This may indicate that the hydrogen is more likely to be found at the oxygen cube positions (at the corners or edge). We discuss the literature data in the context of potential hydrogen transport pathways and how that might be modified by radiation damage, which should be the topic of future investigations. The effect of magnetic ordering on the defect chemistry should also be the focus of future studies.

ACKNOWLEDGMENTS

The authors acknowledge the use of the IRIDIS High Performance Computing Facility, and associated support services at the University of Southampton, in the completion of this work. We are grateful for access to the ARCHER2 national supercomputer which was obtained via the United Kingdom Car-Parrinello Consortium (UKCP) consortium and HE Materials Chemistry Consortium (MCC), funded by EPSRC (Grants No. EP/X035956/1 and No. EP/X035859/1). We are grateful to the UK Materials and Molecular Modelling Hub for computational resources, which is partially funded by EPSRC (Grants No. EP/T022213/1, No. EP/W032260/1, and No. EP/P020194/1), for which access was obtained via the UKCP consortium and funded by EPSRC Grant No. EP/P022561/1. N.A. would also like to thank the CDT for Theory and Modeling the Chemical Sciences (TMCS) (EPSRC Grant No. EP/L015722/1) and AWE for financial support in the form of an ICASE PhD studentship.

[1] I. Grenthe, J. Drożdżyński, T. Fujino, E. C. Buck, T. E. Albrecht-Schmitt, and S. F. Wolf, *The Chemistry of the Actinide and Transactinide Elements*, 4th ed. (Springer, Dordrecht, The Netherlands, 2010), Vol. 1.

[2] H. Matzke, *Radiation Effects in Solids* (Springer, Dordrecht, The Netherlands, 2007).

[3] K. T. Moore and G. van der Laan, Nature of the $5f$ states in actinide metals, Rev. Mod. Phys. **81**, 235 (2009).

[4] L. Dinh, J. M. Haschke, C. K. Saw, P. G. Allen, and W. McLean, II, Pu_2O_3 and the plutonium hydriding process, J. Nucl. Mater. **408**, 171 (2011).

[5] D. Staicu, T. Wiss, V. V. Rondinella, J. P. Hiernaut, R. J. M. Konings, and C. Ronchi, Impact of auto-irradiation on the thermophysical properties of oxide nuclear reactor fuels, J. Nucl. Mater. **397**, 8 (2010).

[6] W. J. Weber, Alpha-irradiation damage in CeO_2, UO_2 and PuO_2, Radiat. Eff. Defects Solids **83**, 145 (1984).

[7] R. Parrish and A. Aitkaliyeva, A review of microstructural features in fast reactor mixed oxide fuels, J. Nucl. Mater. **510**, 644 (2018).

[8] S. L. Dudarev, Density functional theory models for radiation damage, Annu. Rev. Mater. Res. **43**, 35 (2013).

[9] S. Grieshammer, Influence of the lattice constant on defects in cerium oxide, Phys. Chem. Chem. Phys. **20**, 19792 (2018).

[10] J. M. Haschke and T. H. Allen, Plutonium hydride, sesquioxide and monoxide monohydride: pyrophoricity and catalysis of plutonium corrosion, J. Alloys Compd. **320**, 58 (2001).

[11] B. Ao, R. Qiu, H. Lu, and P. Chen, Differences in the existence states of hydrogen in UO_2 and PuO_2 from DFT+U calculations, J. Phys. Chem. C **120**, 18445 (2016).

[12] S. C. Hernandez and E. F. Holby, DFT+U study of chemical impurities in PuO_2, J. Phys. Chem. C **120**, 13095 (2016).

[13] L. Zhang, B. Sun, Q. Zhang, H. Liu, K. Liu, and H. Song, First-principles study of the hydrogen resistance mechanism of PuO_2, ACS Omega **5**, 7211 (2020).

[14] N. Goldman, L. Zepeda-Ruiz, R. G. Mullen, R. K. Lindsey, C. H. Pham, L. E. Fried, and J. L. Belof, Estimates of quantum tunneling effects for hydrogen diffusion in PuO_2, Appl. Sci. **12**, 11005 (2022).

[15] C. K. Saw, J. M. Haschke, P. G. Allen, W. Mclean, II, and L. N. Dinh, Hydrogen corrosion of plutonium: Evidence for fast grain-boundary reaction and slower intragrain reaction, J. Nucl. Mater. **429**, 128 (2012).

[16] G. W. McGillivray, J. P. Knowles, I. M. Findlay, and M. J. Dawes, The plutonium/hydrogen reaction: The pressure dependence of reaction initiation time and nucleation rate controlled by a plutonium dioxide over-layer, J. Nucl. Mater. **412**, 35 (2011).

[17] M. Brierley, J. P. Knowles, A. Sherry, and M. Preuss, The anisotropic growth morphology and microstructure of plutonium hydride reaction sites, J. Nucl. Mater. **469**, 145 (2016).

[18] M. N. Huda and A. K. Ray, A density functional study of atomic hydrogen adsorption on plutonium layers, Phys. B (Amsterdam) **352**, 5 (2004).

[19] M. N. Huda and A. K. Ray, An *ab initio* study of H_2 interaction with the Pu (100) surface, Phys. B (Amsterdam) **366**, 95 (2005).

[20] B. Sun, H. Liu, H. Song, G. Zhang, H. Zheng, X.-G. Zhao, and P. Zhang, The different roles of Pu-oxide overlayers in the hydrogenation of Pu-metal: an *ab initio* molecular dynamics study based on van der Waals density functional (vdW-DF)+U, J. Chem. Phys. **140**, 164709 (2014).

[21] S. S. Hecker and J. C. Martz, Aging of plutonium and its alloys, Los Alamos Sci. **26**, 238 (2000).

[22] J. M. Haschke, T. H. Allen, and L. A. Morales, Surface and corrosion chemistry of plutonium, Los Alamos Sci. **26**, 252 (2000).

[23] J. M. Haschke, T. H. Allen, and L. A. Morales, Reaction of plutonium dioxide with water: Formation and properties of PuO_{2+x}, Science **287**, 285 (2000).

[24] C. E. McNeilly, The electrical properties of plutonium oxides, J. Nucl. Mater. **11**, 53 (1964).

[25] M. Idiri, T. Le Bihan, S. Heathman, and J. Rebizant, Behavior of actinide dioxides under pressure: UO_2 and ThO_2, Phys. Rev. B **70**, 014113 (2004).

[26] T. M. McCleskey, E. Bauer, Q. Jia, A. K. Burrell, B. L. Scott, S. D. Conradson, A. Mueller, L. Roy, X. Wen, G. E. Scuseria *et al.*, Optical band gap of NpO_2 and PuO_2 from optical absorbance of epitaxial films, J. Appl. Phys. **113**, 013515 (2013).

[27] G. Raphael and R. Lallement, Susceptibilite magnetique de PuO_2, Solid State Commun. **6**, 383 (1968).

[28] S. Kern, C.-K. Loong, G. L. Goodman, B. Cort, and G. H. Lander, Crystal-field spectroscopy of PuO_2: further complications in actinide dioxides, J. Phys.: Condens. Matter **2**, 1933 (1990).

[29] S. Kern, R. A. Robinson, H. Nakotte, G. H. Lander, B. Cort, P. Watson, and F. A. Vigil, Crystal-field transition in PuO_2, Phys. Rev. B **59**, 104 (1999).

[30] Y. Tokunaga, H. Sakai, T. Fujimoto, R. E. Walstedt, K. Ikushima, H. Yasuoka, D. Aoki, Y. Homma, Y. Haga, T. D. Matsuda *et al.*, NMR studies of actinide dioxides, J. Alloys Compd. **444-445**, 241 (2007).

[31] H. Yasuoka, G. Koutroulakis, H. Chudo, S. Richmond, D. K. Veirs, A. I. Smith, E. D. Bauer, J. D. Thompson, G. D. Jarvinen,

and D. L. Clark, Observation of ^{239}Pu nuclear magnetic resonance, Science **336**, 901 (2012).
[32] G. Jomard, B. Amadon, F. Bottin, and M. Torrent, Structural, thermodynamic, and electronic properties of plutonium oxides from first principles, Phys. Rev. B **78**, 075125 (2008).
[33] P. Zhang, B.-T. Wang, and X.-G. Zhao, Ground-state properties and high-pressure behavior of plutonium dioxide: Density functional theory calculations, Phys. Rev. B **82**, 144110 (2010).
[34] D. Gryaznov, E. Heifets, and D. Sedmidubsky, Density functional theory calculations on magnetic properties of actinide compounds, Phys. Chem. Chem. Phys. **12**, 12273 (2010).
[35] Y. Yang, B. Wang, and P. Zhang, Electronic and mechanical properties of ordered (Pu, U)O_2 compounds: A density functional theory +*U* study, J. Nucl. Mater. **433**, 345 (2013).
[36] X.-D. Wen, R. L. Martin, G. E. Scuseria, S. P. Rudin, and E. R. Batista, A screened hybrid DFT study of actinide oxides, nitrides, and carbides, J. Phys. Chem. C **117**, 13122 (2013).
[37] P. S. Ghosh and A. Arya, First-principles study of phase stability, electronic and mechanical properties of plutonium sub-oxides, Phys. Chem. Chem. Phys. **21**, 16818 (2019).
[38] J. T. Pegg, A. E. Shields, M. T. Storr, A. S. Wills, D. O. Scanlon, and N. H. de Leeuw, Hidden magnetic order in plutonium dioxide nuclear fuel, Phys. Chem. Chem. Phys. **20**, 20943 (2018).
[39] H. L. Skriver, O. K. Andersen, and B. Johansson, Calculated bulk properties of the actinide metals, Phys. Rev. Lett. **41**, 42 (1978).
[40] A. J. Freeman and G. H. Lander, *Handbook on the Physics and Chemistry of the Actinides* (Elsevier, Amsterdam, 1987), Vol. 5.
[41] N. Cooper, *Challenges in Plutonium Science* (Los Alamos National Laboratory, Los Alamos, NM, 2000), Vol. 26.
[42] G. H. Lander, Sensing electrons on the edge, Science **301**, 1057 (2003).
[43] P. Hohenberg and W. Kohn, Inhomogeneous electron gas, Phys. Rev. **136**, B864 (1964).
[44] W. Kohn and L. J. Sham, Self-consistent equations including exchange and correlation effects, Phys. Rev. **140**, A1133 (1965).
[45] I. D. Prodan, G. E. Scuseria, J. A. Sordo, K. N. Kudin, and R. L. Martin, Lattice defects and magnetic ordering in plutonium oxides: a hybrid density-functional-theory study of strongly correlated materials, J. Chem. Phys. **123**, 014703 (2005).
[46] C. Adamo and V. Barone, Toward reliable density functional methods without adjustable parameters: The PBE0 model, J. Chem. Phys. **110**, 6158 (1999).
[47] J. Heyd, G. E. Scuseria, and M. Ernzerhof, Hybrid functionals based on a screened Coulomb potential, J. Chem. Phys. **118**, 8207 (2003).
[48] I. D. Prodan, G. E. Scuseria, and R. L. Martin, Covalency in the actinide dioxides: Systematic study of the electronic properties using screened hybrid density functional theory, Phys. Rev. B **76**, 033101 (2007).
[49] V. I. Anisimov, J. Zaanen, and O. K. Andersen, Band theory and Mott insulators: Hubbard *U* instead of Stoner *I*, Phys. Rev. B **44**, 943 (1991).
[50] A. I. Liechtenstein, V. I. Anisimov, and J. Zaanen, Density-functional theory and strong interactions: Orbital ordering in Mott-Hubbard insulators, Phys. Rev. B **52**, R5467(R) (1995).
[51] S. L. Dudarev, G. A. Botton, S. Y. Savrasov, C. J. Humphreys, and A. P. Sutton, Electron-energy-loss spectra and the structural stability of nickel oxide: An LSDA+U study, Phys. Rev. B **57**, 1505 (1998).
[52] B. Sun, P. Zhang, and X.-G. Zhao, First-principles local density approximate +*U* and generalized gradient approximate +*U* study of plutonium oxides, J. Chem. Phys. **128**, 084705 (2008).
[53] S. Minamoto, M. Kato, K. Konashi, and Y. Kawazoe, Calculations of thermodynamic properties of PuO_2 by the first-principles and lattice vibration, J. Nucl. Mater. **385**, 18 (2009).
[54] A. B. Shick, J. Kolorenč, L. Havela, T. Gouder, and R. Caciuffo, Nonmagnetic ground state of PuO_2, Phys. Rev. B **89**, 041109(R) (2014).
[55] M. Freyss, N. Vergnet, and T. Petit, *Ab initio* modeling of the behavior of helium and xenon in actinide dioxide nuclear fuels, J. Nucl. Mater. **352**, 144 (2006).
[56] X. Tian, T. Gao, C. Lu, J. Shang, and H. Xiao, First principle study of the behavior of helium in plutonium dioxide, Eur. Phys. J. B **86**, 1 (2013).
[57] Y. Lu, Y. Yang, and P. Zhang, Charge states of point defects in plutonium oxide: A first-principles study, J. Alloys Compd. **649**, 544 (2015).
[58] C. Freysoldt, J. Neugebauer, and C. G. Van de Walle, Fully *ab initio* finite-size corrections for charged-defect supercell calculations, Phys. Rev. Lett. **102**, 016402 (2009).
[59] C. Freysoldt, B. Grabowski, T. Hickel, J. Neugebauer, G. Kresse, A. Janotti, and C. G. Van de Walle, First-principles calculations for point defects in solids, Rev. Mod. Phys. **86**, 253 (2014).
[60] C. W. M. Castleton and S. Mirbt, Ab initio study of neutral vacancies in InP using supercells and finite size scaling, Phys. B (Amsterdam) **340-342**, 407 (2003).
[61] C. W. M. Castleton and S. Mirbt, Finite-size scaling as a cure for supercell approximation errors in calculations of neutral native defects in InP, Phys. Rev. B **70**, 195202 (2004).
[62] C. W. M. Castleton, A. Höglund, and S. Mirbt, Density functional theory calculations of defect energies using supercells, Modelling Simul. Mater. Sci. Eng. **17**, 084003 (2009).
[63] C.-K. Skylaris, P. D. Haynes, A. A. Mostofi, and M. C. Payne, Introducing ONETEP: Linear-scaling density functional simulations on parallel computers, J. Chem. Phys. **122**, 084119 (2005).
[64] J. C. A. Prentice, J. Aarons, J. C. Womack, A. E. A. Allen, L. Andrinopoulos, L. Anton, R. A. Bell, A. Bhandari, G. A. Bramley, R. J. Charlton *et al.*, The ONETEP linear-scaling density functional theory program, J. Chem. Phys. **152**, 174111 (2020).
[65] W. Kohn, Density functional and density matrix method scaling linearly with the number of atoms, Phys. Rev. Lett. **76**, 3168 (1996).
[66] E. Prodan and W. Kohn, Nearsightedness of electronic matter, Proc. Natl. Acad. Sci. USA **102**, 11635 (2005).
[67] C.-K. Skylaris, A. A. Mostofi, P. D. Haynes, O. Diéguez, and M. C. Payne, Nonorthogonal generalized Wannier function pseudopotential plane-wave method, Phys. Rev. B **66**, 035119 (2002).
[68] A. A. Mostofi, P. D. Haynes, Chris-Kriton Skylaris, and M. C. Payne, Preconditioned iterative minimization for linear-scaling electronic structure calculations, J. Chem. Phys. **119**, 8842 (2003).
[69] H. L. Yu, G. Li, H. B. Li, R. Z. Qiu, H. Huang, and D. Q. Meng, Adsorption and dissociation of H_2 on PuO_2 (110) surface: A

density functional theory study, J. Alloys Compd. **654**, 567 (2016).
[70] J. P. Perdew, K. Burke, and M. Ernzerhof, Generalized gradient approximation made simple, Phys. Rev. Lett. **77**, 3865 (1996).
[71] S. J. Clark, M. D. Segall, C. J. Pickard, P. J. Hasnip, M. I. J. Probert, K. Refson, and M. C. Payne, First principles methods using CASTEP, Z. Kristallogr. **220**, 567 (2005).
[72] H. J. Monkhorst and J. D. Pack, Special points for Brillouin-zone integrations, Phys. Rev. B **13**, 5188 (1976).
[73] M. Cococcioni and S. de Gironcoli, Linear response approach to the calculation of the effective interaction parameters in the LDA+U method, Phys. Rev. B **71**, 035105 (2005).
[74] See Supplemental Material at http://link.aps.org/supplemental/10.1103/PhysRevB.xx.xxxxxx Raw data are available at https://doi.org/10.17632/7v6gc7bz34.1 containing the input files including the calculation parameters and the output files with the optimized structures.
[75] B. Amadon, F. Jollet, and M. Torrent, γ and β cerium: LDA+U calculations of ground-state parameters, Phys. Rev. B **77**, 155104 (2008).
[76] J. P. Allen and G. W. Watson, Occupation matrix control of d- and f-electron localisations using DFT+U, Phys. Chem. Chem. Phys. **16**, 21016 (2014).
[77] J.-L. Chen and N. Kaltsoyannis, DFT+U study of uranium dioxide and plutonium dioxide with occupation matrix control, J. Phys. Chem. C **126**, 11426 (2022).
[78] I. C. Njifon, M. Bertolus, R. Hayn, and M. Freyss, Electronic structure investigation of the bulk properties of uranium-plutonium mixed oxides (U, Pu)O_2, Inorg. Chem. **57**, 10974 (2018).
[79] N. Anwar, R. M. Harker, M. T. Storr, M. Molinari, and C.-K. Skylaris, Linear-scaling density functional theory (DFT) simulations of point, Frenkel and Schottky defects in CeO_2, Comput. Mater. Sci. **229**, 112396 (2023).
[80] G. A. Baraff and M. Schlüter, Electronic structure, total energies, and abundances of the elementary point defects in GaAs, Phys. Rev. Lett. **55**, 1327 (1985).
[81] S. B. Zhang and J. E. Northrup, Chemical potential dependence of defect formation energies in GaAs: Application to Ga self-diffusion, Phys. Rev. Lett. **67**, 2339 (1991).
[82] W. Huang and H. Chen, Investigation of the elastic, hardness, and thermodynamic properties of actinide oxides, Phys. B (Amsterdam) **449**, 133 (2014).
[83] P. Martin, S. Grandjean, C. Valot, G. Carlot, M. Ripert, P. Blanc, and C. Hennig, XAS study of $(U_{1-y}Pu_y)O_2$ solid solutions, J. Alloys Compd. **444-445**, 410 (2007).
[84] J.-P. Dancausse, E. Gering, S. Heathman, and U. Benedict, Pressure-induced phase transition in ThO_2 and PuO_2, High Press. Res. **2**, 381 (1990).
[85] Elastic constants, https://github.com/andreww/elastic-constants.
[86] M. Born, On the stability of crystal lattices, Math. Proc. Cambridge Philos. Soc. **36**, 160 (1940).
[87] A. M. Ganose, A. J. Jackson, and D. O. Scanlon, sumo: Command-line tools for plotting and analysis of periodic *ab initio* calculations, J. Open Source Software **3**, 717 (2018).
[88] P. R. L. Keating, D. O. Scanlon, B. J. Morgan, N. M. Galea, and G. W. Watson, Analysis of intrinsic defects in CeO_2 using a Koopmans-like GGA+U approach, J. Phys. Chem. C **116**, 2443 (2012).
[89] K. P. Huber and G. Herzberg, *Molecular Spectra and Molecular Structure. IV. Constants of Diatomic Molecules* (Van Nostrand Reinhold, New York, 1979).
[90] M. Freyss and T. Petit, *Ab initio Modelling of the Behaviour of Helium in Americium and Plutonium Oxides* (ATALANTE, Nimes, France, 2004), pp. 1–6.
[91] S. Singh, Y. Sonvane, K. A. Nekrasov, A. Y. Kupryazhkin, P. N. Gajjar, and S. K. Gupta, A first principles investigation of defect energetics and diffusion in actinide dioxides, J. Nucl. Mater. **591**, 154901 (2024).
[92] C. J. Cramer, W. B. Tolman, K. H. Theopold, and A. L. Rheingold, Variable character of O—O and M—O bonding in side-on (η^2) 1:1 metal complexes of O_2, Proc. Natl. Acad. Sci. USA **100**, 3635 (2003).
[93] S. Moxon, J. Skelton, J. S. Tse, J. Flitcroft, A. Togo, D. J. Cooke, E. L. da Silva, R. M. Harker, M. T. Storr, S. C. Parker *et al.*, Structural dynamics of Schottky and Frenkel defects in ThO_2: a density-functional theory study, J. Mater. Chem. A **10**, 1861 (2022).
[94] T. Smith, S. Moxon, J. S. Tse, J. M. Skelton, D. J. Cooke, L. J. Gillie, E. L. da Silva, R. M. Harker, M. T. Storr, S. C. Parker *et al.*, Structural dynamics of Schottky and Frenkel defects in CeO_2: a density-functional theory study, J. Phys. Energy **5**, 025004 (2023).
[95] Y. Yun and W. W. Kim, First principle studies on electronic and defect structures of UO_2, ThO_2, and PuO_2, in *Transactions of the Korean Nuclear Society, Jeju, Korea* (2007).
[96] H. Nakamura and M. Machida, A first-principles study on point defects in plutonium dioxide, Prog. Nucl. Sci. Technol. **5**, 132 (2018).
[97] W. D. Neilson, J. T. Pegg, H. Steele, and S. T. Murphy, The defect chemistry of non-stoichiometric $PuO_{2\pm x}$, Phys. Chem. Chem. Phys. **23**, 4544 (2021).
[98] P. A. Burr and M. W. D. Cooper, Importance of elastic finite-size effects: Neutral defects in ionic compounds, Phys. Rev. B **96**, 094107 (2017).